Full-Spectrum Utilization of ZIF-67/Ag NPs/NaYF$_4$:Yb,Er Photocatalysts for Efficient Degradation of Sulfadiazine: Upconversion Mechanism and DFT Calculation

Weijin Yang, Cheng Bu, Min Zhao, Yafei Li, Shihai Cui, Jing Yang,* and Hongzhen Lian**

In this work, novel ternary composite ZIF-67/Ag NPs/NaYF$_4$:Yb,Er is synthesized by solvothermal method. The photocatalytic activity of the composite is evaluated by sulfadiazine (SDZ) degradation under simulated sunlight. High elimination efficiency of the composite is 95.4% in 180 min with good reusability and stability. The active species (h$^+$, ·O$_2$$^-$ and ·OH) are identified. The attack sites and degradation process of SDZ are deeply investigated based on theoretical calculation and liquid chromatography-mass spectrometry analysis. The upconversion mechanism study shows that favorable photocatalytic effectiveness is attributed to the full utilization of sunlight through the energy transfer upconversion process and fluorescence resonance energy transfer. Additionally, the composite is endowed with outstanding light-absorbing qualities and effective photogenerated electron–hole pair separation thanks to the localized surface plasmon resonance effect of Ag nanoparticles. This work can motivate further design of novel photocatalysts with upconversion luminescence performance, which are applied to the removal of sulphonamide antibiotics in the environment.

1. Introduction

Antibiotics are widely used in human and veterinary medicine for their excellent properties in treating bacterial infections.[1] Because of broad antibacterial spectrum, sulphonamide antibiotics have been synthesized and utilized worldwide. Sulfadiazine (SDZ) is a classic sulphonamide antibiotic.[2] It is one of the most frequently utilized antibiotics and excellent antibacterial agent in animal husbandry medicine.[3,4] Despite the low levels in the environment, it may cause drug resistance in some pathogenic bacteria. Moreover, due to the misuse, the SDZ concentration improved gradually. In the report, the average concentration in Huixian karst wetland reached a maximum of 48.24 μg·L^{-1} in Guilin, China.[5] Hence, it is imperative to find a cost-effective method to remove SDZ residue. So far, some technologies, such as photocatalysis,[6] Fenton,[7] ozone,[8] persulfate[9,10] and biodegradation,[11] have been applied to the removal of organic contaminants. One of the most efficient and environmentally favorable of these is photocatalysis. The creation of effective photocatalysts has become a popular area of study recently.

Metal–organic framework (MOF) is a new type of porous coordination polymer made up of organic ligands and metal nodes that are used in various fields due to their abundant active sites, high specific surface area and tunable structure.[12–14] In the field of photocatalysis, some MOFs are commonly used semiconductors-like including Materials Institute Lavoisier (MIL),[15] Universitetet i Oslo (UiO)[16] and Zeolitic Imidazolate Frameworks (ZIF).[17] Among them, ZIF materials have attracted a lot of attentions not only because they are thermally and chemically stable,[18] but also for the reasons that the ligand bridge of ZIF is liable to transfer the charge from the organic linker to the metal ions at the connecting node.[19] With a suitable bandgap, ZIF-67 displays unique optical absorption characteristics.[20] Nevertheless, its photocatalytic performance needs to be enhanced due to the poor separation and transfer efficiency of photogenerated carriers.[21] To solve the problem, the composition of noble metal nanoparticles (NMNPs) and MOFs is an excellent strategy. The addition of NMNPs can improve photocatalytic performance via the localized surface plasmon resonance effect (LSPR). Liang et al. synthesized Pd@MIL-100(Fe) for effective photocatalytic degradation of bisphenol A, ibuprofen and theophylline.[22] Khan et al. used ZIF-67/Au-PCN ternary nanocomposites in the high active decontamination of bisphenol A (BPA) under simulated visible light irradiation.[23] Notably, the addition of Au tunes the bandgap of the material

---

W. Yang, C. Bu, M. Zhao, Y. Li, S. Cui, J. Yang
Jiangsu Collaborative Innovation Center of Biomedical Functional Materials
Jiangsu Key Laboratory of Biomedical Materials
School of Chemistry and Materials Science
Jiangsu Provincial Key Laboratory of Materials Cycling and Pollution Control
Nanjing Normal University
Nanjing 210023, China
E-mail: cuishihai@njnu.edu.cn; chemyangjing@njnu.edu.cn

H. Lian
State Key Laboratory of Analytical Chemistry for Life Science
School of Chemistry & Chemical Engineering and Center of Materials Analysis
Nanjing University
Nanjing 210023, China
E-mail: hzlian@nju.edu.cn

The ORCID identification number(s) for the author(s) of this article can be found under https://doi.org/10.1002/smll.202309972

DOI: 10.1002/smll.202309972

through the surface plasmon resonance (SPR) effect. A fly in the ointment of NMNPs@MOFs is the relatively low utilization of sunlight. The solar spectrum, as everybody knows, is composed of 52% near infrared light (700–2500 nm), 43% visible light (400–700 nm), and 5% UV light (300–400 nm).[24] Most of the NMNPs@MOFs can response to UV–vis illumination without the absorption of near-infrared light.

Upconversion nanoparticle (UCNPs), as a unique material, has Anti-Stokes effect. It can successively absorb two or more low-energy, long-wavelength excitation light photons (e.g. near-infrared light) and radiate short-wavelength, high-energy emission light photons (e.g. visible light, UV light).[25] UCNPs have three components: matrix material, activator and sensitizer. In general, oxides, fluorides, hydroxides, vanadates, and phosphates are frequently employed as matrix materials. Considering the phonon energy and structural stability of the material, fluoride is the best upconversion matrix material that is currently widely researched and applied.[26] Rare earth ions are always used as activator and sensitizer.[27] Yb^{3+} has a relatively simple energy level structure and only one excited state ($^2F_{5/2}$) of 4f energy level. Compared with other rare earth ions, Yb^{3+} absorption cross-section is larger. So it is a good sensitizer.[28] Er^{3+} is commonly used as an activator because of its abundance of long-lived intermediate state energy levels.[29] Prior to now, UCNPs are frequently employed in fluorescent labeling, imaging and biomedical.[30] So far, the application of upconversion materials in photocatalysis is still in its early stages. Zhu et al. discovered that $NaYF_4$:Yb,Er@CdS showed 14.8 times enhancement of photocatalytic hydrogen precipitation in visible-near-infrared light compared to the pristine cubic CdS.[31] In addition, the upconversion emission can be enhanced when the UCNPs is combined with NMNPs. Wang et al. found that appropriately sized Ag nanoparticles could enhance the luminescence effect of $NaYF_4$:Yb/Er.[32] Niu et al. discovered that when β-$NaYF_4$:Yb,Tm was compounded with the precious metal Au. The upconversion emission intensity located at 291 and 345 nm increased significantly under near-infrared light irradiation.[33] Hence, there is a strong interaction between UCNPs and NMNPs. The synergistic effect between NMNPs@MOFs and UCNPs via fluorescence resonance energy transfer (FRET) enables NMNPs@MOFs to further absorb the UV–vis light emitted by UCNPs. Based on the pre-experiments by our group, it is found that the match between emitted light of UCNPs and absorbed light of semiconductor is important for the full utilization of sunlight.

In this work, a simple solvothermal method was used to generate a novel ZIF-67/Ag NPs/$NaYF_4$:Yb,Er photocatalyst. The crystal structure, morphology, surface chemical composition and state, chemical structure and optical properties were characterized. The photocatalytic performance of all composites for SDZ degradation was investigated by using simulated sunlight irradiation. The ZIF-67/Ag NPs/$NaYF_4$:Yb,Er composite's stability and reusability were confirmed. During SDZ degradation process, the active species, photocatalytic mechanism, and degradation routes were also deeply analyzed. Besides these, the primary goals of this effort are: 1) To verify that there is a good degree of match between ZIF-67/Ag absorbed light and $NaYF_4$:Yb,Er emitted light range; 2) To determine the contribution of noble metal nanoparticles to the separation effect of electron–hole pairs; 3) To explore the feasibility of improving solar light utilization with upconversion materials. Therefore, this work not only shows a photocatalyst for efficient removal of SDZ, but also provides a fresh perspective on how sulfonamide antibiotics are degraded by photocatalysis.

2. Experimental Section

2.1. Chemicals

All chemical reagents are analytically pure without further purification. Polyvinyl pyrrolidone (PVP), 2-methylimidazole, benzoquinone (BQ), silver nitrate ($AgNO_3$), and sodium fluoride (NaF) were purchased from Macklin Biochemical Technology Limited Company (Shanghai, China). Sulfadiazine (SDZ), yttrium chloride (YCl_3) and ytterbium chloride ($YbCl_3$) were obtained from Aladdin Reagents Limited Company (Shanghai, China). The following chemicals were purchased from Sinopharm Chemical Reagent Company (Shanghai, China): sodium chloride (NaCl), sodium hydroxide (NaOH), ethylene glycol, cobalt nitrate hexahydrate ($Co(NO_3)_2 \cdot 6H_2O$), isopropanol (IPA), erbium chloride ($ErCl_3$), ethylenediaminetetraacetic acid disodium (EDTA-2Na) and methanol. Purified water from Wahaha Group Company (Hangzhou, China) was used in the experiments.

2.2. Preparation of Catalyst

2.2.1. Preparation of $NaYF_4$:Yb,Er

$NaYF_4$:Yb,Er was synthesized by the following steps with some modifications.[34] EDTA-2Na (0.7445 g, 2 mmol) was dispersed into 20 mL of aqueous solution $LnCl_3$, which contained $ErCl_3$ (0.0109 g, 0.04 mmol), $YbCl_3$ (0.1550 g, 0.4 mmol) and YCl_3 (0.4732 g, 1.56 mmol). The metal-EDTA complex (solution A) was formed under vigorous stirring. Meanwhile, solution B was created by dissolving appropriate amount of NaF (0.504 g, 12 mmol) in 20 mL of purified water. Then, solution A and solution B were mixed and agitated magnetically for 30 min. The mixture above underwent a specified quantity of NaOH addition until the solution pH reached 5.0 with continuous magnetic stirring for 30 min at 25 °C. Thereafter, they were put into a 50 mL Teflon-lined steel autoclave and heated at 180 °C for 10 h. After the reaction, the $NaYF_4$:Yb,Er material was acquired by centrifugation, washing and drying. The ratios of the reactants are $LnCl_3$:EDTA-2Na:NaF = 1:1:6, Y:Yb:Er = 39:10:1.

2.2.2. Preparation of ZIF-67/$NaYF_4$:Yb,Er

In order to fabricate ZIF-67/$NaYF_4$:Yb,Er, 80 mL of methanol were ultrasonically combined with 100 mg of $NaYF_4$:Yb,Er and $Co(NO_3)_2 \cdot 6H_2O$ (0.1164 g, 0.4 mmol)to produce solution C. Additionally, 2-methylimidazole (0.2463 g, 3 mmol) were sonicated to dissolve into 20 mL of methanol solution in order to get solution D. Solution D was added to solution C and stirring magnetically for 24 h at 60 °C. After the reaction, the ZIF-67/$NaYF_4$:Yb,Er composite material was obtained by centrifugation, washing and drying.

For comparison, ZIF-67 nanomaterial has been produced using the same procedure without the inclusion of $NaYF_4$:Yb,Er.[35]

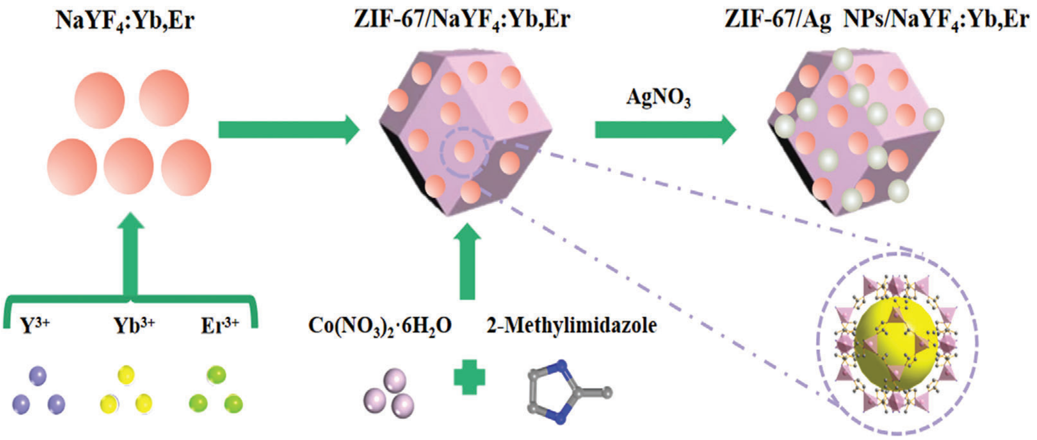

Figure 1. Schematic diagram of the synthesis of ZIF-67/Ag NPs/$NaYF_4$:Yb,Er.

2.2.3. Preparation of ZIF-67/Ag NPs/$NaYF_4$:Yb,Er

ZIF-67/Ag NPs/$NaYF_4$:Yb,Er was prepared using a simple solvothermal method. First, 0.2 g of ZIF-67@$NaYF_4$:Yb,Er, 0.13875 g of PVP and $AgNO_3$ (0.0425 g, 0.25 mmol) were added sequentially to 20 mL of ethylene glycol and stirred magnetically for 30 min. Afterward, NaCl (0.002 g, 0.03 mmol) was dispersed into the mixture with ultrasonic treatment. The solution was then put into a 70 mL Teflon-lined steel autoclave and remained at 160 °C for 4 h. After cooling to room temperature, ZIF-67/Ag NPs/$NaYF_4$:Yb,Er composites were collected through centrifugation, washing and then dried. The Ag NPs were prepared similarly without the addition of ZIF-67@$NaYF_4$:Yb,Er. The schematic diagram for the synthesis was shown in **Figure 1** below.

2.3. Photocatalytic Evaluation

The XPA-7 photocatalytic device (Xujiang Electromechanical Plant, Nanjing, China) with 500 W xenon as simulated sunlight was utilized during photocatalysis process. In the experiment, 15 mg catalyst was dispersed into 30 mL of SDZ solution (10 mg L^{-1}). The suspension was magnetically agitated in the dark for 1 h before illumination to establish adsorption–desorption equilibrium. When light was available, 1.0 mL of the solution was sampled at a certain time and filtered through a 0.22 µm membrane. High performance liquid chromatography (HPLC) was then applied to determine concentration of the target on a Waters 1525, USA.

2.4. Photoelectrochemical Measurements

The electrochemical impedance spectra (EIS), Mott–Schottky (M–S) measurements and transient photocurrent response (TPC) were obtained on an electrochemical workstation (CHI-660E, Shanghai Chenhua Instruments Co., Ltd.). The measurement procedure makes use of a typical three-electrode system. Pt wire serves as the counter electrode; Ag-AgCl performs as the reference electrode; the working electrode is the catalyst deposited on the F-doped Tin Oxide (FTO) conductive glass.

2.5. Density Functional Theory Calculations

The Materials Studio 7.0 program, based on first principle and density function theory (DFT), was used to model and optimize molecular structures. The Cartesian coordinates of the SDZ structure were obtained after geometric optimization by Forcite and B3LYP generalized functions, and the optimized coordinates were continued for quantitative simulation calculations employing both DMoL3 and CASTEP modules. The potential SDZ degradation sites and pathways were ascertained mainly based on the calculation results of Mulliken electron layout number, the bond order, the HOMO-LUMO orbital, the condensed Fukui function, the reduced double descriptor and the electrostatic potential, etc.

3. Results and Discussion

3.1. Characterization

3.1.1. Morphology and Microstructure Analysis

Transmission electron microscopy (TEM) and scanning electron microscopy (SEM) were adopted to examine the morphology and size of the produced materials. $NaYF_4$:Yb,Er are uniform nanospheres with the size 50–100 nm, which can be observed in **Figure 2A**. ZIF-67 is truncated rhombic dodecahedron with the size ≈500 nm (Figure 2B). The fact that Ag NPs and $NaYF_4$:Yb,Er are uniformly distributed on the surface of ZIF-67 in the SEM and TEM images of Figure 2C,D shows that the composite ZIF-67/Ag NPs/$NaYF_4$:Yb,Er was successfully manufactured. HR-TEM images of ZIF-67/Ag NPs/$NaYF_4$:Yb,Er are shown in Figure 2E. The lattice spacing of 0.237 and 0.317 nm corresponds to the (111) crystal plane of Ag NPs and $NaYF_4$, respectively, which further substantiates the successful loading of Ag NPs on the surface of ZIF-67. The energy-dispersive X-ray spectroscopy (EDX) in Figure 2F shows that the elements C, N, O, Co, Ag, Na, Y, F, Yb, and Er coexist in the composite. The mapping diagram in Figure S1 (Supporting Information) further demonstrates that the above elements are uniformly dispersed in the ZIF-67/Ag NPs/$NaYF_4$:Yb,Er composites.

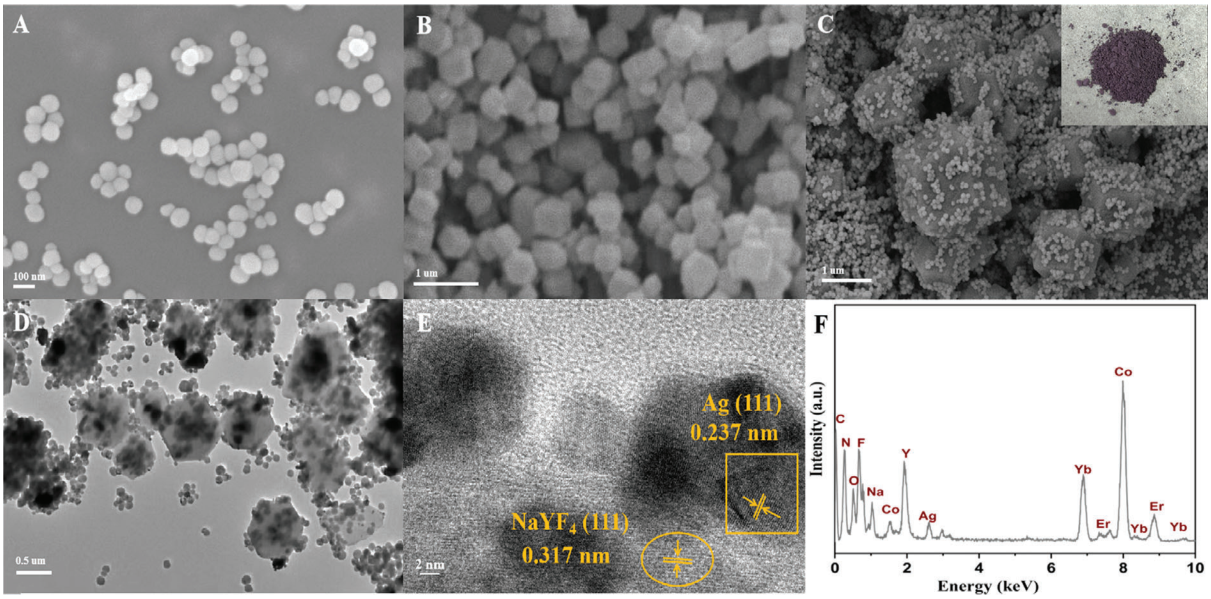

Figure 2. The SEM images of NaYF$_4$:Yb,Er (A), ZIF-67 (B) and ZIF-67/Ag NPs/NaYF$_4$:Yb,Er (C, with a photo on the top-right); The TEM (D) and HR-TEM (E) images of ZIF-67/Ag NPs/NaYF$_4$:Yb,Er; The EDS spectrum of ZIF-67/Ag NPs/NaYF$_4$:Yb,Er (F).

3.1.2. XRD Analysis

The crystal structure of the prepared material was examined using an X-ray diffraction (XRD) pattern in **Figure** 3A. The diffraction peaks for NaYF$_4$:Yb,Er observed at $2\theta = 28.1°$, 32.5°, 46.8°, 55.4°, 58.1°, and 68.5° match the standard PDF card (JCPDS: 77–2042) of the cubic phase for (111), (200), (220), (311) (222) and (400) crystallographic planes.[34,36] It is demonstrated that the synthesis of the α-phase NaYF$_4$:Yb,Er was successful. The diffraction signals of ZIF-67 at 7.3°, 10.5°, 12.8°, 18.1°, 22.1°, 24.6°, 26.5°, and 29.7° are in agreement with the previously reported data, indicating good crystallinity.[37,38] The decrease in peak intensity of ZIF-67 when it is mixed with NaYF$_4$:Yb,Er may be attributed to the partial breakage of the Co—N bond and the affect of MOF crystallinity.[39,40] The Ag NPs has the characteristic peaks at 38.1°, 44.3°, 64.2°, and 77.3°, which is in accordance with the PDF card (JCPDS: 04–0783).[41,42,43] Obviously, the above signals can be found in the composite, which proves the synthesis of ternary material ZIF-67/Ag NPs/NaYF$_4$:Yb,Er.

3.1.3. FT-IR Analysis

FT-IR is effective method to characterize changes in functional groups of materials, which provides useful information related

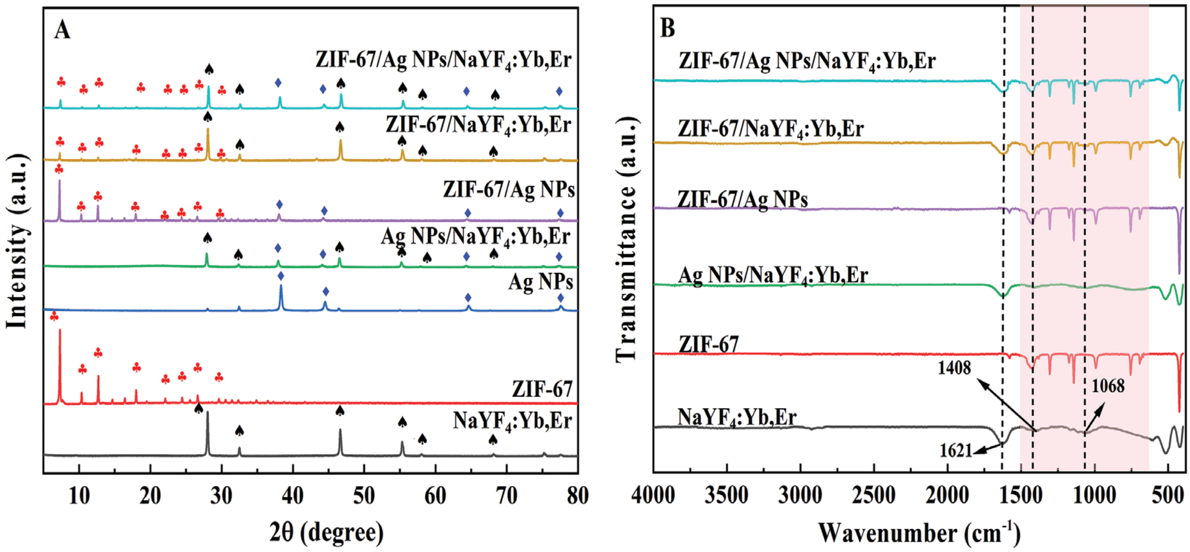

Figure 3. XRD patterns (A) and FT-IR spectra (B) of the produced materials.

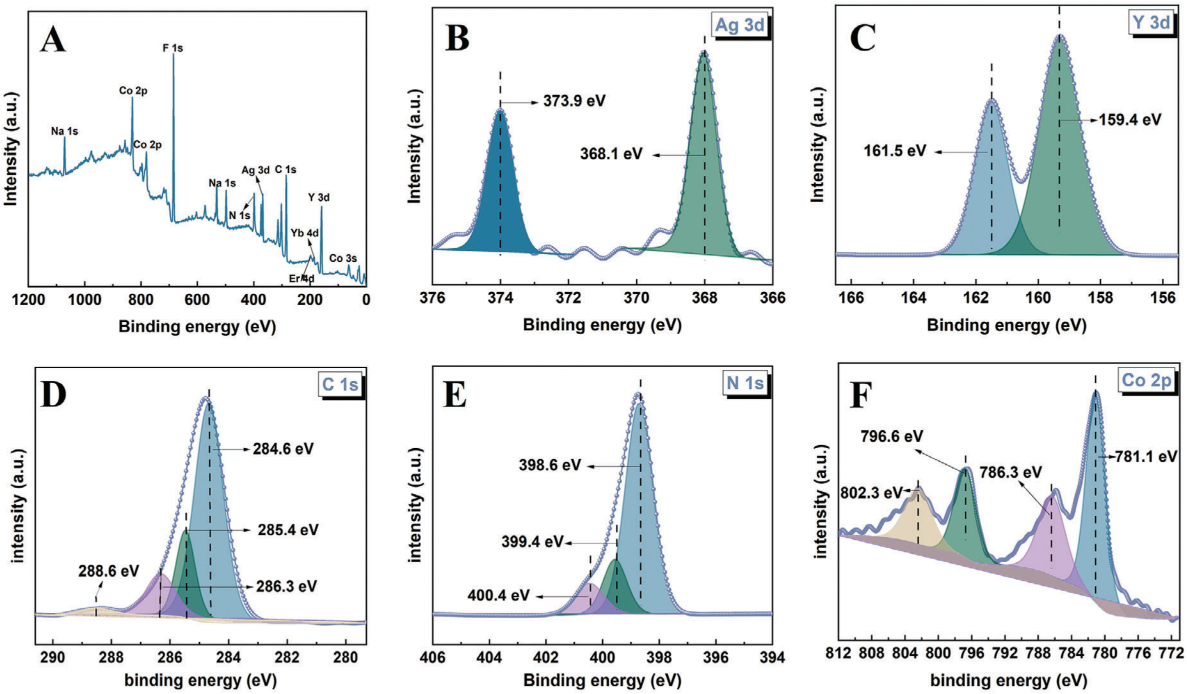

Figure 4. The XPS survey spectra of ZIF-67/Ag NPs/NaYF$_4$:Yb,Er (A) and XPS high-resolution scans of Ag 3d (B); Y 3d (C); C 1s (D); N 1s (E) and Co 2p (F).

to molecular vibrational modes. In ZIF-67 contained spectra in Figure 3B, the vibrational peaks at 600–1600 cm^{-1} are the stretching and bending vibrations of the imidazole ring in ZIF-67.[37] In the spectrum of NaYF$_4$:Yb,Er, it can be viewed that the characteristic absorption peaks at 1621 and 1068 cm^{-1} coincident to the stretching and deformation vibrations of the C—N bond, respectively. And the broad peak at 1408 cm^{-1} belongs to the vibrational absorption band of —COOH in EDTA-2Na.[34] It is indicated that NaYF$_4$:Yb,Er was successfully prepared. The characteristic peaks above can all be found in ZIF-67/Ag NPs/NaYF$_4$:Yb,Er, which shows that the introduction of Ag NPs did not destroy the structure and the composite was well prepared.

3.1.4. XPS Analysis

X-ray photoelectron spectroscopy (XPS) was used for analyzing the surface chemical composition and elemental states of the prepared materials. **Figure** 4A shows the full scan spectrum, proving the composite consists of the elements Ag, Na, Y, F, Yb, Er, C, N, and Co. Figure 4B displays the high resolution XPS spectra of Ag 3d. The convolution of two binding energy peaks at 368.1 and 373.9 eV corresponds to 3d$_{5/2}$ and 3d$_{3/2}$ of Ag^0, respectively. Na 1s peak is found at binding energy 1072.1 eV (Figure S2A, Supporting Information). The peaks observed at 159.4 and 161.5 eV (Figure 4C) belong to Y 3d$_{5/2}$ and Y 3d$_{3/2}$ of Y^{3+}, respectively.[44,45] The peak at binding energy of 685.1 eV can be attributed to F 1s (Figure S2B, Supporting Information). The two peaks with binding energies of 172.6 and 174.7 eV for Er 4d demonstrate the presence of Er^{3+} (Figure S2C, Supporting Information). Similarly, the peak with a binding energy of 186.2 eV is attributed to the presence of Yb^{3+} (Figure S2D, Supporting Information).[46] The C1s spectrum can be fitted to three peaks at 284.6, 285.4, 286.3, and 288.6 eV, which can be considered as C=C, C—C, C=N, and O=C—O (Figure 4D).[47] In Figure 4E, the three binding energies at 398.6, 399.4, and 440.4 eV represent pyrrole nitrogen, pyridine nitrogen and graphitic nitrogen, respectively. Moreover, the peaks at 781.1 and 796.6 eV obtained by convolution in Figure 4F correspond to Co 2p$_{3/2}$ and 2p$_{1/2}$, respectively, while the peaks at 786.3 and 802.3 eV are the accompanying satellite peaks.[37] Generally speaking, the energy gap between the Co 2p main peaks and their corresponding satellite peaks can be used as an important criterion to determine the oxidation state of cobalt in XPS spectra. The binding energy of Co (II) is ≈6.0 eV and the Co (III) is usually 9–10 eV.[48,49] In Figure 4F, the binding energy are calculated to be 5.2 and 5.7 eV, which indicates the existence of Co (II).

3.2. Evaluation of Photocatalytic Activity and Stability

3.2.1. Photocatalytic Degradation of SDZ

Different Catalysts: The photocatalytic activity of ZIF-67/Ag NPs/NaYF$_4$:Yb,Er catalyst was evaluated via photodegradation of SDZ under the irradiation of simulated sunlight. Before each catalysis, SDZ was mixed with the material without illumination till the adsorption equilibrium was reached (Figure S3, Supporting Information). The photodegradation performance of SDZ by various materials is depicted in **Figure** 5A. When monomer upconversion material NaYF$_4$:Yb,Er was used, the SDZ is hardly degraded. The ZIF-67 has the better effect with

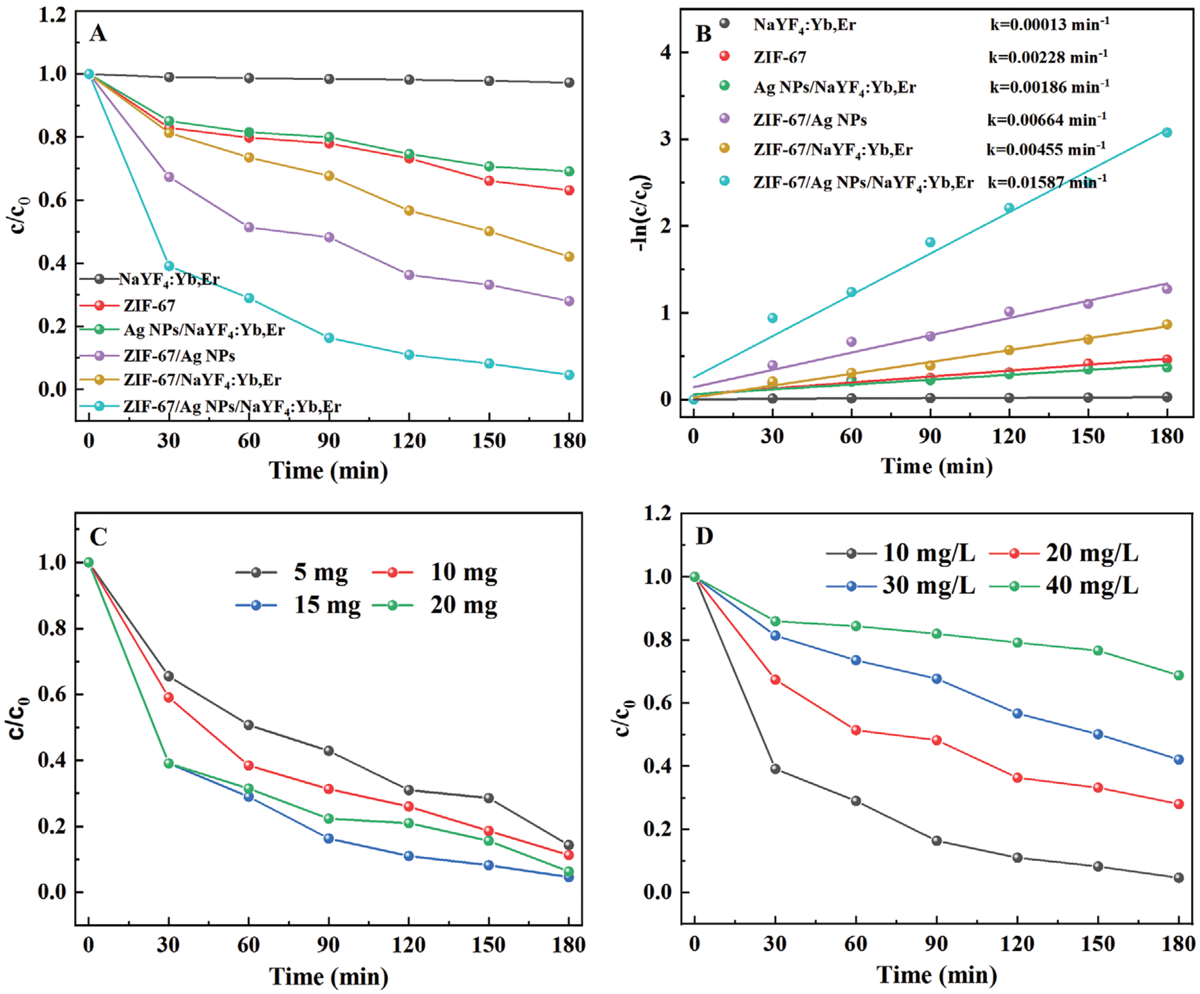

Figure 5. Photocatalytic degradation of SDZ by all materials (A); Pseudo-first-order reaction kinetics of SDZ by different catalysts (B); Influence of ZIF-67/Ag NPs/NaYF$_4$:Yb,Er dosage (C) and effect of SDZ concentration (D).

the degradation efficiency of 36.9%. In the binary materials, ZIF-67/Ag NPs has the best effect of 72%, owing to the introduction of Ag. Particularly, ZIF-67/Ag NPs/NaYF$_4$:Yb,Er has the optimal photocatalytic activity. After 180 min' illumination, ≈95.4% of SDZ was removed. This may be due to the fact that the ternary material can efficiently and fully utilize the simulated sunlight. In which, ZIF-67 and Ag NPs in ternary materials are able to absorb and utilize the UV and visible light for photocatalysis. The electrons in the upconversion material NaYF$_4$:Yb,Er can be excited by near-infrared light to generate radiation and energy transfer then to produce visible light, which is reabsorbed by ZIF-67/Ag NPs and utilized for subsequent photocatalysis. This layered broad-spectrum absorption mode greatly enhances the photocatalytic degradation performance of SDZ. In addition, the reaction kinetics of SDZ was studied. According to Equations 1–3, the kinetics analysis of synthesized materials is shown in Figure 5B. The correlation coefficient (R^2) of ZIF-67/Ag NPs/NaYF$_4$:Yb,Er is 0.9773. It shows that the process was in accordance with pseudo-first-order kinetics. ZIF-67/Ag NPs/NaYF$_4$:Yb,Er has the largest reaction rate constant k, 0.01587 min^{-1}, which is 6.96 times higher than that of ZIF-67. The relative parameters are listed in Table S1 (Supporting Information).

$$r_t = -\frac{dC_t}{dt} = k_n C_t^n \tag{1}$$

$$C_t = C_0 \exp(-kt) \tag{2}$$

$$\ln C_t = -kt + \ln C_0 \tag{3}$$

where, r is the reaction rate, C_0 represents the initial concentration, C_t is the concentration at time t, n is reaction order, k is rate constant.

Moreover, the prepared ZIF-67/Ag NPs/NaYF$_4$:Yb,Er is superior or comparable with the materials reported before (Table S2, Supporting Information).[50–55]

Catalysts Dosage: One of the important parameters influencing photocatalytic efficiency is catalyst dosage. Figure 5C shows that the SDZ degradation effect improves from 85.7% to 95.4% when the amount of catalyst varied from 5 to 15 mg, for the

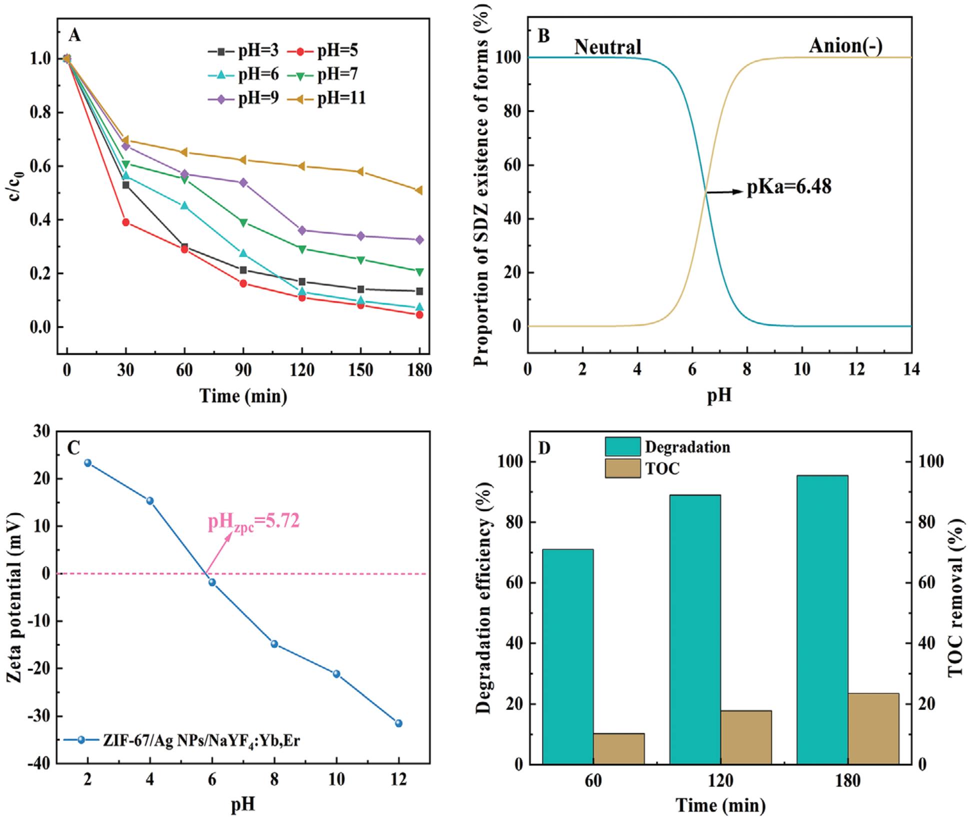

Figure 6. Impact of initial pH on SDZ degradation (A), the morphological distribution of SDZ (B), the zeta potential of ZIF-67/Ag NPs/$NaYF_4$:Yb,Er (C) and photocatalytic degradation efficiency and TOC removal efficiency of SDZ by the ZIF-67/Ag NPs/$NaYF_4$:Yb,Er (D).

reason of more degradation active sites and free radicals. However, when the dosage increased from 15 to 20 mg, the SDZ removal decreased slightly. When too much catalyst is added, the ZIF-67/Ag NPs/$NaYF_4$:Yb,Er particles tend to aggregate and reduce the light transmittance. Thus restricted the photocatalytic activity. So 15 mg of catalyst was the ideal dosage.

SDZ Concentration: The impact of incipient SDZ concentration on photodegradation efficiency is depicted in Figure 5D. The degradation efficiency gradually reduced from 95.4% (10 $mg{\cdot}L^{-1}$) to 26.2% (40 $mg{\cdot}L^{-1}$) when the SDZ concentration raised from 10 to 40 $mg{\cdot}L^{-1}$. During the reaction, the SDZ with high concentration can produce more intermediates, which competed with SDZ for active radicals and hampered the effective degradation. Therefore, 10 $mg{\cdot}L^{-1}$ solution was selected for the experiment.

Effect of Initial pH: The solution pH has a significant effect on the photocatalytic activity of the material. The effect of solution pH for photocatalytic activity of ZIF-67/Ag NPs/$NaYF_4$:Yb,Er was investigated. **Figure** 6A shows that the degradation of SDZ increased from pH 3.0 to 5.0 and decreases from pH 5.0 to 11.0. The optimal degradation took place in weakly acidic solutions. When pH 5, the degradation efficiency was 95.4%, and when pH 6, the degradation efficiency was 92.7%. This result was closely related to the acid dissociation constant (pKa) in Figure 6B and isoelectric point of SDZ in Figure 6C. From the morphological distribution, SDZ existed mainly as neutral molecule at pH <6.48 and anion at pH> 6.48.[56] Figure 6C demonstrates the isoelectric point of ZIF-67/Ag NPs/$NaYF_4$:Yb,Er at ≈5.72. The material had a positive surface charge at pH <5.72 and a negative surface charge at pH> 5.72. At pH 3.0, the solution contained less hydroxyl anions, which in turn hinders the production of hydroxyl radicals, thus reduces the decomposition efficiency of SDZ. At pH 5.0–6.0, SDZ molecules gradually ionized and became negatively charged, which made the photodegradation reaction easier by electrostatic attraction with the positively charged catalyst. The presence of a large number of hydroxyl anions leaded to the generation of more hydroxyl radicals, which further increased the degradation efficiency of SDZ. Under alkaline conditions, both the material and the SDZ surface were negatively charged, and the electrostatic repulsion prevented the SDZ from approaching the material surface. Therefore, the photodegradation of SDZ reduced under pH 7.0–11.0. So the best degradation efficiency of SDZ was achieved at pH 5.0.

3.2.2. The Mineralization Efficiency and 3D Excitation-Emission Matrix Fluorescence Spectra

The mineralization capacity is a crucial characteristic to assess the performance of the photocatalyst. In accordance with Figure 6D, the degradation efficiency and mineralization efficiency of ZIF-67/Ag NPs/$NaYF_4$:Yb,Er on SDZ could reach 95.4% and 23.5%, respectively, after 3 h of simulated sunlight irradiation. It was indicated that SDZ was first converted to intermediate products during the photocatalytic degradation process,

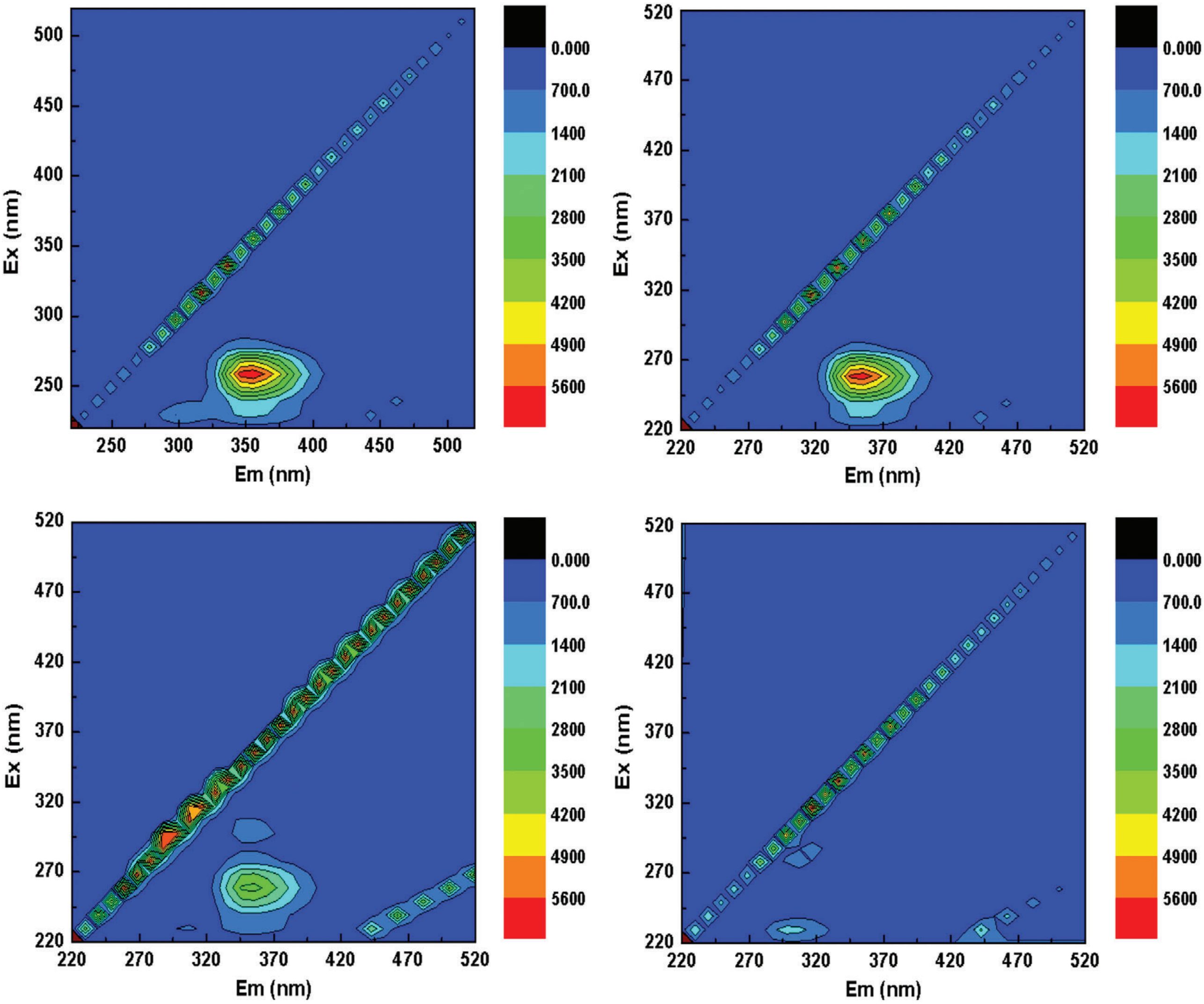

Figure 7. The 3D-EEMs spectra of SDZ original solution (A), after 60 min of adsorption in the dark (B), after 90 min (C) and 180 min (D) of photodegradation by ZIF-67/Ag NPs/NaYF$_4$:Yb,Er.

but only some of the intermediates were mineralized to H_2O and CO_2.

The characteristic peaks of 3D excitation-emission matrix fluorescence spectra (3D-EEMs) are closely related to the structure and functional groups of organic molecules. Therefore, it is used to analyze the transformation process of the molecular structure during the degradation of SDZ. As shown in **Figure** 7A, the characteristic fluorescence peaks showed strong SDZ signal peaks at Em/Ex = 350/260 nm.[57] After 60min of adsorption in the dark (Figure 7B), the intensity of the characteristic peak did not change significantly compared with Figure 7A, indicating that SDZ is relatively stable. Under simulated sunlight irradiation, the intensity of SDZ gradually diminished (Figure 7C). The difference of the fluorescence is very obvious from SDZ molecules to dark adsorption for 60 min, then to light irradiation for 90 min, which is consistent with the experiment results of SDZ degradation in Figure 5A. The fluorescence peak at Em/Ex = 350/300 nm is attributed to tryptophan analogues,[58] and the fluorescence peaks at Em/Ex = 300/230 nm and 310/280 nm are assigned to tyrosine analogues in Figure 7C,D.[57,59,60] After the irradiation of 180 min, SDZ fluorescence peaks almost vanished (Figure 7D). The main reason may be that the conjugated heterocyclic structure of SDZ was destroyed and different intermediates were formed during photocatalytic degradation. Accordingly, 3D-EEMs further confirmed that ZIF-67/Ag NPs/NaYF$_4$:Yb,Er can disrupt the molecular structure of SDZ.

3.2.3. Active Species

The possible active species in ZIF-67/Ag NPs/NaYF$_4$:Yb,Er were further determined by radical trapping experiments. In this work, three scavengers, EDTA-2Na, IPA and BQ were introduced to the catalytic system for the consumption of h^+, $\cdot OH$ and $\cdot O_2^-$, respectively. The active species were captured and then quenched during the process by corresponding scavengers. If the degradation

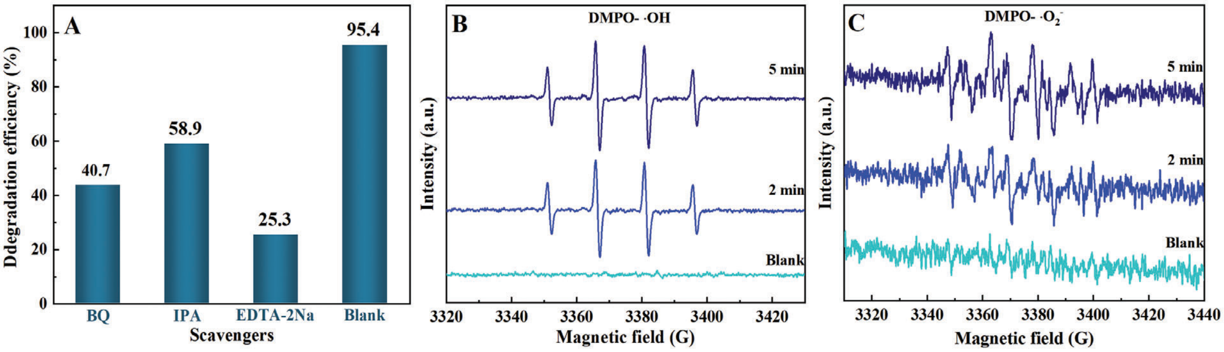

Figure 8. Free radical capture experiment: The effects of different scavengers on SDZ degradation (A); EPR spectra of free radicals using DMPO as spin trapping agent under simulated visible light: trapping ·OH in aqueous solution (B) and $\cdot O_2{}^-$ in methanol solution (C).

efficiency is lower than that without scavengers, it is indicated that the certain free radical plays a role in the degradation process. As depicted in **Figure** 8A, the degradation efficiency of SDZ was ≈95.4% when no scavengers were added. After the addition of EDTA-2Na, IPA and BQ, the SDZ removal efficiency decreased to 25.3%, 58.9% and 40.7%, respectively. Therefore, the degradation of SDZ was significantly inhibited. It means that h^+, ·OH and $\cdot O_2{}^-$ are significant active species leading to the degradation of SDZ in the photocatalytic reaction.

EPR is an electromagnetic spectroscopy method to study magnetic substances containing one or more unpaired electrons. It were performed to further verify the active species generated by ZIF-67/Ag NPs/$NaYF_4$:Yb,Er. As spin trapping agent, the 5,5-dimethyl-1-pyrroline N-oxide (DMPO) is a good candidate. According to Figure 8B,C, no discernible signal was seen in the dark because there was no ·OH and $\cdot O_2{}^-$ generated. Under light, the DMPO-·OH with a 1:2:2:1 quartet peaks could be found distinctly when water was used as solvent.[61] Meanwhile, the characteristic signals of DMPO-$\cdot O_2{}^-$ were detected when methanol was used as solvent. The results of this EPR measurement are basically compatible with the free radical capture experiments.

3.2.4. *Reaction Intermediates, Degradation routes, and DFT Calculation*

To deeply analyze the intermediates produced from SDZ and degradation paths, LC-MS coupling technique was performed with electrospray interface (ESI) source in positive ion mode. The peaks of the intermediates can be apparently observed in Figure S4 (Supporting Information). The structure formulas were determined by comparing the fragment ions detected in LC-MS with those reported in previous studies.[62,63] The mass-to-charge ratios, chemical structures and retention times of the intermediates are described in Table S3 (Supporting Information). The other by-product peaks mainly correspond to some coupled adducts.

The optimized calculation results according to the Cartesian coordinates of SDZ (Table S4, Supporting Information) are displayed in **Figure** 9A. Based on the frontier molecular orbital theory, HOMO and LUMO can be used to describe the positions where organic pollutant molecules are more likely to lose or gain electrons during photodegradation.[64] The HOMO and LUMO orbitals (Figure 9B) of SDZ were focused on the benzene and pyrimidine rings, respectively. It is indicated that the pyrimidine ring is susceptible to nucleophilic attack by $\cdot O_2{}^-$/·OH radicals.[65] The Fukin function is defined as the result of the partial differentiation of the electron density (ρ) at a point (r) in space with respect to the number of electrons. The definition formula is as follows:

$$f(r) = \left(\frac{\partial^2 E}{\partial_N \partial_{v(r)}}\right) = \left(\frac{\partial \mu}{\partial v(r)}\right)_N = \left(\frac{\partial \rho(r)}{\partial N}\right)_{v(r)} \tag{4}$$

where, ρ is the electron density, μ is the chemical potential, r is the positional site vector, N is the number of electrons, and v is the attraction potential of the nucleus for electrons at a given position. N is an integer, so the function is discontinuous. The limit is sought separately from both sides using the finite difference approximation, then Equation 4 is converted to:

$$f^+(r) = \lim_{\varepsilon \to 0^+} \frac{\rho_{N+\varepsilon(r)} - \rho_{N(r)}}{\varepsilon} \tag{5}$$

$$f^-(r) = \lim_{\varepsilon \to 0^-} \frac{\rho_{N(r)} - \rho_{N-\varepsilon(r)}}{\varepsilon} \tag{6}$$

$$f^2(r) = f^+(r) - f^-(r) \tag{7}$$

According to the condensed Fukui function from the Hirshfeld charge distribution calculation, the atomic numbers, f^-, f^+, and f^2 are shown in Figure 9C. From Equation 7, f^- and f^+ together determine the value of the dual descriptor (f^2). Generally speaking, an atom with negative f^2 are susceptible to electrophilic attack, and an atom with positive f^2 are liable to nucleophilic attack. The electrophilic and nucleophile sites were further identified based on the abbreviated double descriptors derived from the abbreviated Fukui function. In the result, C2, C4, C6, O9, C14, and N17 are substantially more negative. The N12, C13, C15, and N16 are comparatively more positive value.[66,67]

In the light of the eight intermediates (Table S3, Supporting Information) found and prior reports,[62,63,67] **Figure 10** depicts the mechanism of SDZ photodegradation. First, in Path I, N17 of SDZ was susceptible to electrophilic attack, which led to the breakage of the N—H bond and the yield of sulfadiazine radicals to form intermediate M1 via a coupling reaction. The S—N bond of M1 was attacked by ·OH to generate P1. Second, in Path II,

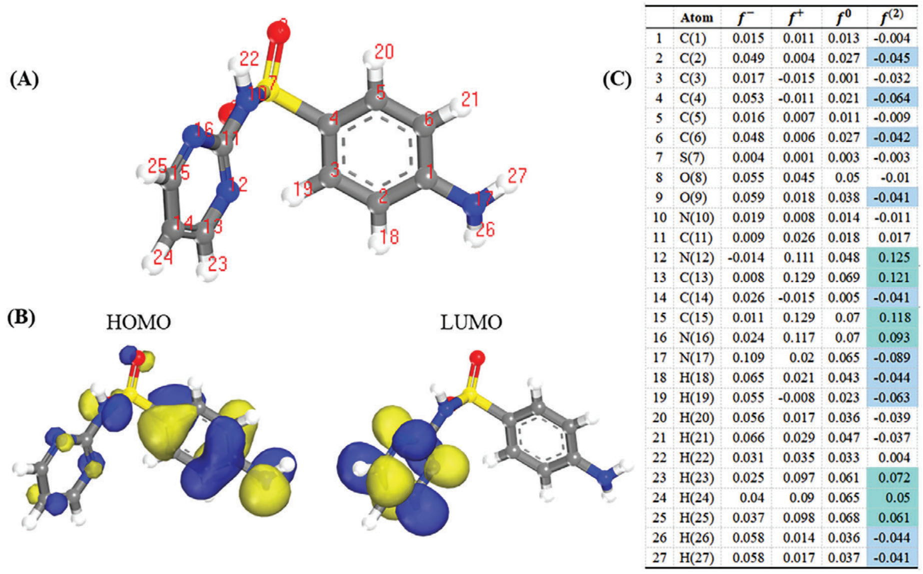

	Atom	f^-	f^+	f^0	$f^{(2)}$
1	C(1)	0.015	0.011	0.013	-0.004
2	C(2)	0.049	0.004	0.027	-0.045
3	C(3)	0.017	-0.015	0.001	-0.032
4	C(4)	0.053	-0.011	0.021	-0.064
5	C(5)	0.016	0.007	0.011	-0.009
6	C(6)	0.048	0.006	0.027	-0.042
7	S(7)	0.004	0.001	0.003	-0.003
8	O(8)	0.055	0.045	0.05	-0.01
9	O(9)	0.059	0.018	0.038	-0.041
10	N(10)	0.019	0.008	0.014	-0.011
11	C(11)	0.009	0.026	0.018	0.017
12	N(12)	-0.014	0.111	0.048	0.125
13	C(13)	0.008	0.129	0.069	0.121
14	C(14)	0.026	-0.015	0.005	-0.041
15	C(15)	0.011	0.129	0.07	0.118
16	N(16)	0.024	0.117	0.07	0.093
17	N(17)	0.109	0.02	0.065	-0.089
18	H(18)	0.065	0.021	0.043	-0.044
19	H(19)	0.055	-0.008	0.023	-0.063
20	H(20)	0.056	0.017	0.036	-0.039
21	H(21)	0.066	0.029	0.047	-0.037
22	H(22)	0.031	0.035	0.033	0.004
23	H(23)	0.025	0.097	0.061	0.072
24	H(24)	0.04	0.09	0.065	0.05
25	H(25)	0.037	0.098	0.068	0.061
26	H(26)	0.058	0.014	0.036	-0.044
27	H(27)	0.058	0.017	0.037	-0.041

Figure 9. The optimized structure (A) of SDZ; HOMO and LUMO orbitals (B) and Fukui indexes (C) of SDZ.

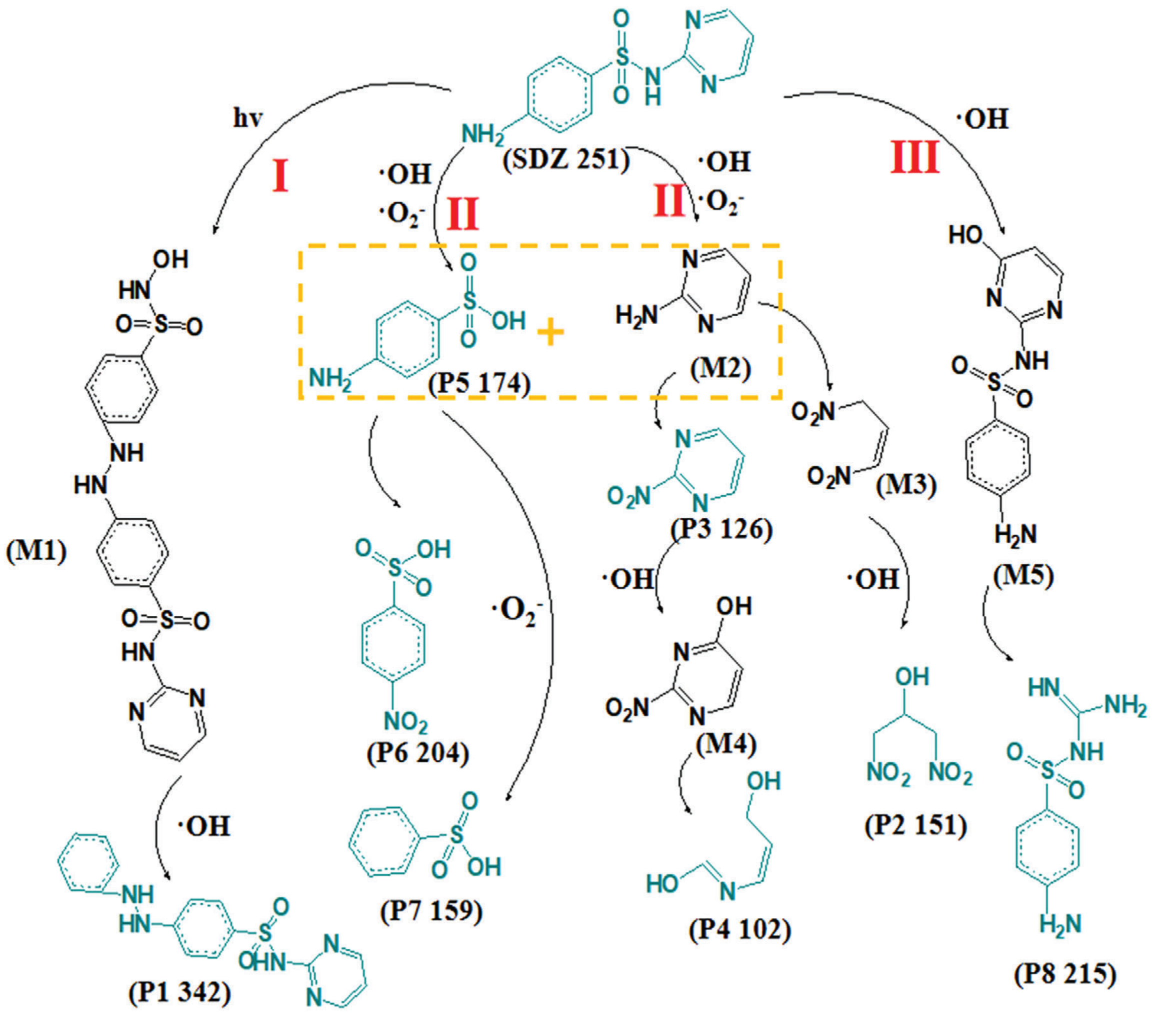

Figure 10. Possible pathways for the degradation of SDZ by ZIF-67/Ag NPs/NaYF$_4$:Yb,Er.

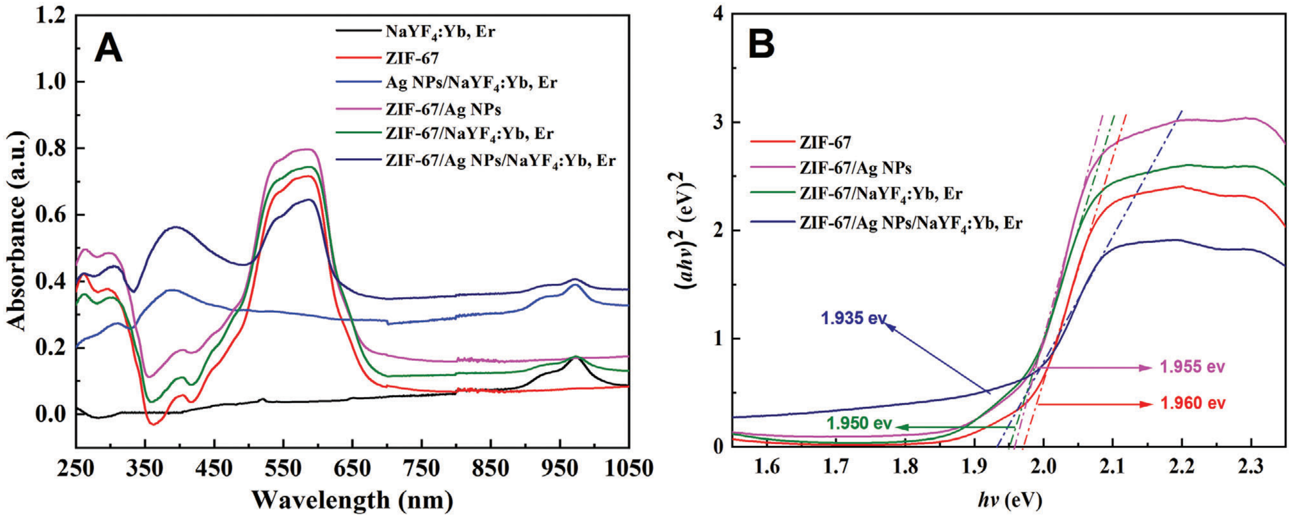

Figure 11. UV–vis–NIR DRS spectra of the synthesized materials (A) and Tauc's plots of $(\alpha h\nu)^2$ versus hv of the materials (B).

SDZ was attacked by ·OH and $\cdot O_2^-$, which caused the break of S—N bond and produced P5 and M2. On the one hand, the amino groups in P5 and M2 are oxidized to nitro groups to yield the products P6 and P3, respectively. P3 was hydroxylated and went through pyrimidine ring-opening to further generate the product P4. P6 was deaminated and oxidized to the product P7. Another aspect, M2 was attacked with active substances to create the oxidative ring-opening product M3, then to P2 after the electrophilic addition reaction of C═C double bond. In addition, in Path III, C13 and C15 are vulnerable to nucleophilic attack according to f^2 equal to 0.121 and 0.118, respectively, producing the hydroxylation product M5. The LUMO diagram of SDZ demonstrated that the pyrimidine ring was easily attacked by the nucleophile, which led to the breakage of the C-N bond and finally generated the product P8.

3.2.5. Recyclability and Stability

To test the reusability of ZIF-67/Ag NPs/NaYF$_4$:Yb,Er in photocatalytic process and its stability in aqueous environment, ten photocatalytic degradation experiments were conducted on the ternary catalyst under simulated sunlight irradiation and the outcomes are displayed in Figure S5A (Supporting Information). It is evident that the degradation effect of SDZ decreased from 95.4% to 72.9%, indicating relatively good material stability. In addition, the XRD patterns and FT-IR spectra of the materials are displayed in Figure S5B,C (Supporting Information) before and after the ten cycles. The signals did not change distinctly, which further indicated that ZIF-67/Ag NPs/NaYF$_4$:Yb,Er has relatively reliable recyclability and stability.

3.3. Investigation of Degradation Mechanisms

3.3.1. Energy Band Structure

The light absorption properties of the materials were examined employing UV–vis–NIR diffuse reflectance spectroscopy (UV–vis–NIR DRS). As illustrated in **Figure 11A**, NaYF$_4$:Yb,Er and their related composites exhibited near-infrared absorption at 975 nm, which is associated with electron transition of Yb^{3+}.[68] Materials containing ZIF-67 all exhibited two sets of absorption bands in the UV–vis light ranges. The signal in the UV region (250–300 nm) can be explained by ligand-to-metal charge transfer (LMCT).[69] The characteristic peaks in the visible range from 500 to 650 nm can be associated with the $^4A_2$ (F)→$^4T_1$ (P) transition of the Co(II) ion in the cobalt–nitrogen tetrahedron, which is defined the triple peak of spin coupling. The characteristic peak at 350–450 nm is assigned to Ag NPs adsorption originated from the localized surface plasmon resonance (LSPR).[70] From the analysis above, the ternary composite can successfully expand the spectral response range from the UV and vis to the NIR range, thereby it enabled the efficient utilization of solar energy during photocatalytic reactions.

Ordinarily, the energy band structure of photocatalyst determines the migration process of electron–hole pairs. The Tauc's diagram (Figure 11B) can be constructed from the curve of $(\alpha h\nu)^2$ to $h\nu$, with the bandgap (E_g) as the intercept between the tangent line and the x-axis according to Tauc's formula (Equation 8):

$$\alpha h\nu = A(h\nu - E_g)^{\frac{n}{2}} \tag{8}$$

where A is a constant; ν is the frequency of light; α is the absorption coefficient near the absorption edge; h is Planck's constant; E_g is the absorption energy bandgap; and $n = 4$ corresponds to indirect bandgap semiconductor. The E_g of ZIF-67/Ag NPs/NaYF$_4$:Yb, Er was only 1.935 eV. Compared with other catalysts, the E_g of the ternary material was significantly narrower, which enabled more light to be utilized. In addition, it hastened the separation and transfer of photoexcited electron–hole pairs.[71]

The M–S tests at various frequencies (**Figure 12A**) were applied to determine the positions of the conduction band (CB) and valence band (VB). The tangent slope of ZIF-67 is positive at different frequencies, demonstrating that it is n-type semiconductor. The intersection of the three tangents with the x-axis was −0.44

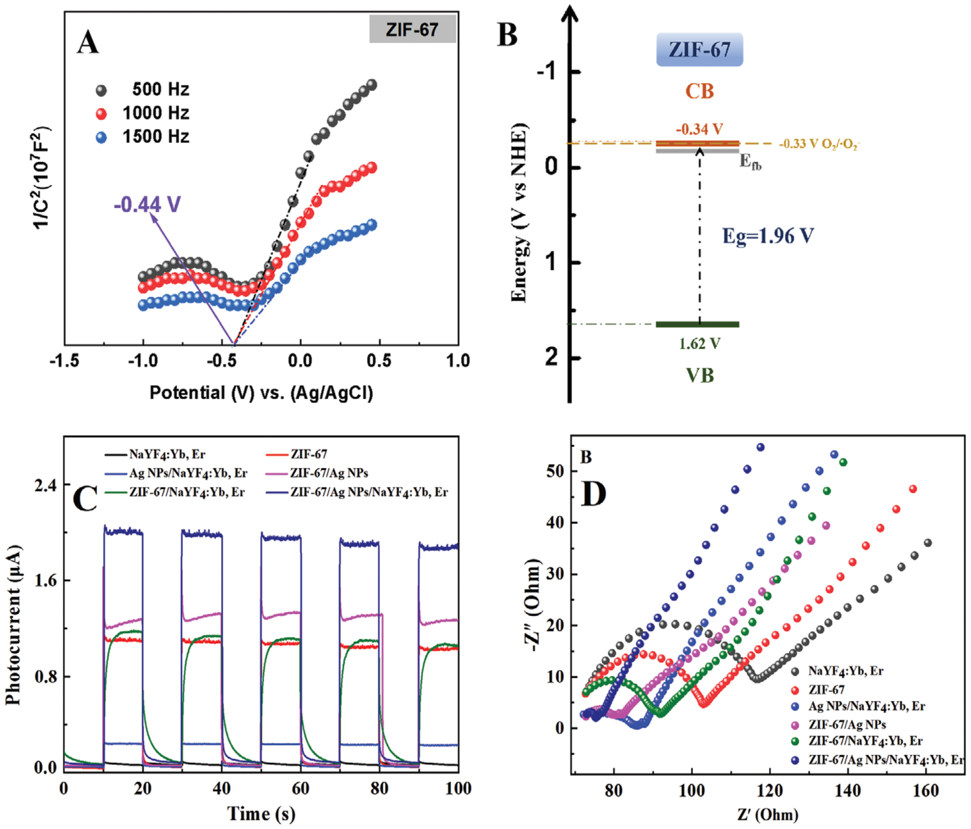

Figure 12. Mott–Schottky test at multiple frequencies of ZIF-67 (A) and band structure diagram of ZIF-67 (B); TPC curves (C) and EIS Nyquist plots (D) of various photocatalytic materials.

eV (vs Ag/AgCl), which is flat-band potential (E_{fb}) of the ZIF-67s. The Equation 9 can be employed to convert E_{fb} (vs Ag/AgCl) to E_{fb} (vs. NHE), which is −0.24 eV (vs NHE).[72] Generally speaking, the E_{CB} of *n*-type semiconductors is 0.1 eV less than E_{fb}.[73] According to the Equation 10 and the rational energy band structure diagram in Figure 12B, the E_{CB} is −0.34 eV and E_{VB} is 1.62 eV. The VB-XPS of ZIF-67 is shown in Figure S6 (Supporting Information).

$$E_{fb}\left(vsNHE\right) = Efb\left(vsAg/AgCl\right) + 0.2 \tag{9}$$

$$E_{VB} = E_{CB} + E_g \tag{10}$$

3.3.2. Photogenerated Carrier

The electrochemical analysis including TPC and EIS were conducted to examine the utilization of e^--h^+ couples. The photocurrent response spectra of various materials are displayed in Figure 12C. Apparently, the ternary composite exhibited a steady and continuous photocurrent response in five cycles. The electric current is much higher than those of other materials, illustrating that the ZIF-67/Ag NPs/$NaYF_4$:Yb,Er composite has more efficient carrier separation efficiency and stronger photocatalytic activity. The EIS analysis is presented in Figure 12D. Rct is the resistance to electron transport between the electrode surface and the material on the electrode surface. In Nyquist plot, Rct is calculated by the diameter of the semicircle.[74] From this, Rct = 44.91 Ω ($NaYF_4$:Yb,Er); 30.75 Ω (ZIF-67); 13.00 Ω (Ag NPs/$NaYF_4$:Yb,Er); 7.50 Ω (ZIF-67/Ag NPs); 20.25 Ω (ZIF-67/$NaYF_4$:Yb,Er); 2.75 Ω (ZIF-67/Ag NPs/$NaYF_4$:Yb,Er). It is noticeable that the ternary ZIF-67/Ag NPs/$NaYF_4$:Yb,Er catalyst has the minimum arc radius, which represents the lowest interfacial charge transfer resistance and the quickest electron transfer rate. [75]

3.3.3. Exploration of Mechanism

The upconversion mechanism of $NaYF_4$:Yb,Er nanoparticles can be visually described by the energy level schematics of Yb^{3+} and Er^{3+}. In **Figure 13A**, the electron in the ground state $^2F_{7/2}$ of the sensitizer Yb^{3+} are motivated to the excited state $^2F_{5/2}$ by near-infrared photons (980 nm). Partial of the excited electron returns to the ground state of Yb^{3+} by radiation or energy transfer. The other part of the energy is transferred to Er^{3+}, which induces the excitation of Er^{3+} electrons through energy transfer upconversion process (ETU). The electrons on the $^4I_{15/2}$ ground state are excited to $^4I_{11/2}$ state through the process: $^4I_{15/2}(Er^{3+})+^2F_{5/2}(Yb^{3+})\rightarrow{}^4I_{11/2}(Er^{3+})+^2F_{7/2}(Yb^{3+})$. Subsequently, the electrons transit to the $^4I_{13/2}$ state by non-radiative relaxation. Accompanying the energy supply from Yb^{3+}, it is transferred to $^4F_{9/2}$ states. With $^4F_{9/2}$ relaxation to the ground level, red emission centered at 659 nm

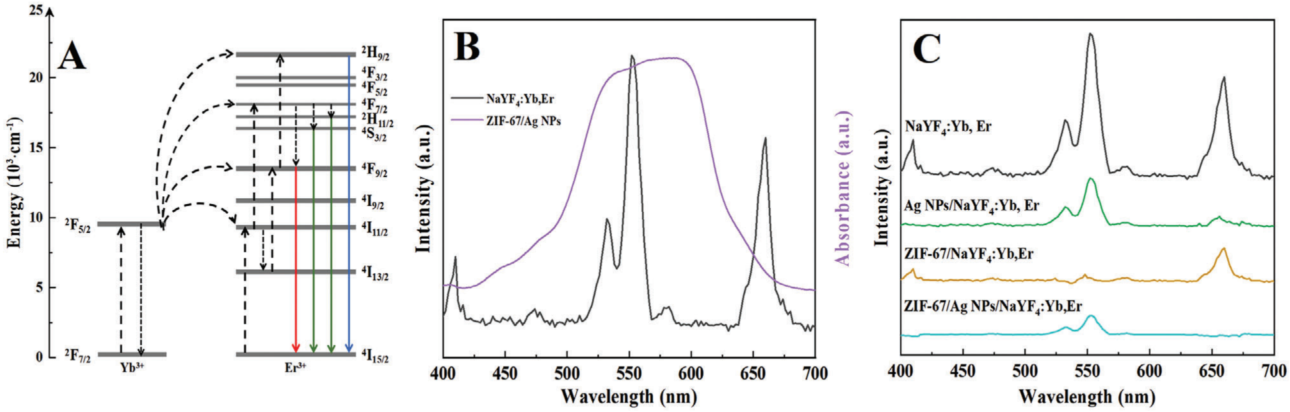

Figure 13. Energy level diagram of Yb^{3+} and Er^{3+} energy transfer (A); UV–vis DRS spectra of ZIF-67/Ag NPs and the upconversion fluorescence emission spectra of NaYF$_4$:Yb,Er (B); Upconversion fluorescence emission spectra under the excitation at 980 nm for different materials (C).

occurs.[76] Similarly, the electrons on the $^4F_{9/2}$ are further excited to $^2H_{9/2}$ state by following the energy transfer process: $^4F_{9/2}(Er^{3+})+^2F_{5/2}(Yb^{3+})\rightarrow^2H_{9/2}(Er^{3+})+^2F_{7/2}(Yb^{3+})$, which is accompanied by the appearance of blue light at 410 nm.[77,78] The non-radiation relaxation occupies the $^2H_{11/2}$ and $^4S_{3/2}$ states, which can emit green light (527 and 548 nm) when the electrons are transferred to the ground state $^4I_{15/2}$.[79]

The upconversion emission spectra of NaYF$_4$:Yb,Er and the UV–vis diffuse reflectance spectra of ZIF-67/Ag NPs under the excitation of 980 nm are exhibited in Figure 13B. It is illustrated that NaYF$_4$:Yb,Er can absorb near-infrared light (NIR) and produce visible light with the main peaks at 410, 527, 548, and 659 nm, respectively corresponding to blue, green, green, and red light mentioned in Figure 13A, respectively. ZIF-67/Ag NPs have good light absorption between 450–680 nm. Therefore, there is an excellent spectral overlap between the NaYF$_4$:Yb,Er and ZIF-67/Ag NPs. The light that NaYF$_4$:Yb,Er emits can exactly be absorbed by ZIF-67/Ag NPs. The unique performance can be used for photocatalysis effectively.[78,80]

The upconversion emission spectra of different materials were further measured. Four emission peaks of NaYF$_4$:Yb,Er respectively correspond to the $^2H_{9/2}\rightarrow^4I_{15/2}$ (410 nm), $^2H_{11/2}\rightarrow^4I_{15/2}$ (527 nm), $^4S_{3/2}\rightarrow^4I_{15/2}$ (548 nm) and $^4F_{9/2}\rightarrow^4I_{15/2}$ (659 nm) transition of Er^{3+}. After the introduction of Ag NPs into the material, the peaks at 410 and 659 nm gradually reduced, showing the blue and red light emitted by the NaYF$_4$:Yb,Er are absorbed by Ag NPs. After the composition with ZIF-67, the peaks at 527 and 548 nm get weaker, indicating the green light emitted by the NaYF$_4$:Yb,Er are absorbed by ZIF-67. The spectral changes in Figure 13C reflect the energy transfer between NaYF$_4$:Yb,Er and other components. Thereafter, the near-infrared light from the sunlight can be used in upconversion composite.

The photocatalytic mechanism of ZIF-67/Ag NPs/NaYF$_4$:Yb,Er can be elaborated based on the band theory, carrier transmission, upconversion spectrum and active species. According to spectral analysis, only the UV and visible light from the simulated sunlight can be absorbed by ZIF-67/Ag NPs. In the ternary composite, NaYF$_4$:Yb,Er can absorb the near-infrared light through ETU process and then emit visible light through anti-Stokes shift luminescence process. Partial light (green) was then absorbed by ZIF-67, while the other (red and blue light) absorbed by Ag NPs. Thus, the composite made full use of the full spectrum of simulated sunlight. Additionally, an effective FRET process occurred between NaYF$_4$:Yb,Er and ZIF-67/Ag NPs with NaYF$_4$:Yb,Er as the energy donor and ZIF-67/Ag NPs as the acceptor. FRET can be understood as the process of energy transfer from the donor to the acceptor. The spectral changes in Figure 13C can unambiguously reflect the energy transfer between NaYF$_4$:Yb,Er and ZIF-67/Ag NPs. In detail, NaYF$_4$:Yb,Er is excited by infrared light (980 nm) and emits visible light (410, 527, 548, and 659 nm), which is absorbed by ZIF-67/Ag NPs. Therefore, the energy is successfully transferred to ZIF-67/Ag NPs. More than that, Ag NPs made the important effect in light adsorption due to the LSPR function. Based on the photoelectric properties, the ZIF-67/Ag NPs/NaYF$_4$:Yb,Er has the optimal carrier separation efficiency and the lowest electron–hole recombination rate. All the characters above promote the outstanding photocatalytic performance. Under the irradiation, ZIF-67/Ag NPs/NaYF$_4$:Yb,Er is excited to produce e^- and h^+, which reacted with O_2 and H_2O and then generated $\cdot O_2^-$ and $\cdot OH$. The active species h^+, $\cdot O_2^-$ and $\cdot OH$ gradually decomposed the SDZ to produce the intermediates and finally produce CO_2 and H_2O. The schematic expression of the photodegradation is exhibited in **Figure 14**.

4. Conclusion

In brief, novel ternary composite ZIF-67/Ag NPs/NaYF$_4$:Yb,Er was successfully synthesized by facile solvothermal method and employed to degrade SDZ under simulated sunlight. The degradation efficiency of SDZ by ZIF-67/Ag NPs/NaYF$_4$:Yb,Er composite reached 95.4% within 180 min. The reaction rate of ZIF-67/Ag NPs/NaYF$_4$:Yb,Er was 6.96 times more than that of the pristine ZIF-67, which was attributed to not only the adsorption of broad spectra of sunlight including NIR and UV–vis light, but also the high charge separation efficiency of the composite. Furthermore, the ZIF-67/Ag NPs/NaYF$_4$:Yb,Er demonstrated exceptional structural stability and reusability. The main active species is $\cdot O_2^-$, $\cdot OH$, and h^+ in the photocatalytic process. DFT calculation and LC-MS analysis were employed to predict the intermediates and pathways. Not only does this work offer promising insights into the upconversion material for enhancing

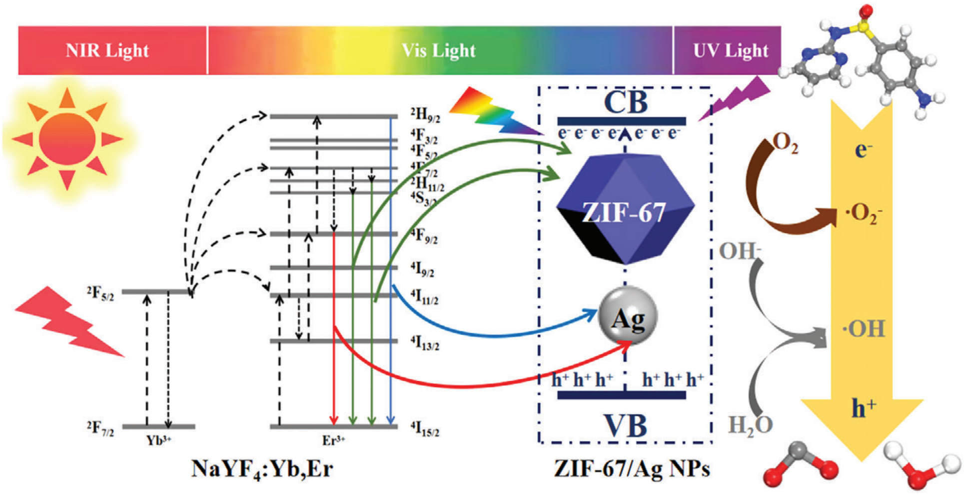

Figure 14. Diagram of ZIF-67/Ag NPs/NaYF$_4$:Yb,Er photocatalytic degradation mechanism.

photocatalytic degradation, but also gives an innovative way for the preparation of highly active catalyst in the application of photodegradation.

Supporting Information

Supporting Information is available from the Wiley Online Library or from the author.

Acknowledgements

This work was supported by the National Natural Science Foundation of China (21177061, 91643105, 21874065, and 22176085), Natural Science Foundation of Jiangsu Province (BK20150968).

Conflict of Interest

The authors declare no conflict of interest.

Data Availability Statement

The data that support the findings of this study are available from the corresponding author upon reasonable request.

Keywords

mechanism, photodegradation, sulfadiazine, upconversion material, ZIF-67/Ag NPs/NaYF$_4$:Yb,Er

Received: November 2, 2023
Revised: January 8, 2024
Published online: January 26, 2024

---

[1] Z. Q. Zhang, J. L. Liang, W. Zhang, M. Zhou, X. L. Zhu, Z. Y. Liu, Y. Li, Z. Q. Guan, C. S. Lee, P. K. Wong, H. M. Li, Z. F. Jiang, *Appl. Catal. B* **2023**, *330*, 122621.
[2] X. Chen, F. Deng, X. Liu, K. P. Cui, R. Weerasooriya, *Sci. Total Environ.* **2021**, *774*, 145776.
[3] M. Conde-Cid, D. Fernández-Calviño, J. C. Nóvoa-Muñoz, M. Arias-Estévez, M. Díaz-Raviña, A. Núñez-Delgado, M. J. Fernández-Sanjurjo, E. Álvarez-Rodríguez, *J. Environ. Manage.* **2018**, *228*, 239.
[4] W. Baran, E. Adamek, A. Sobczak, A. Makowski, *Appl. Catal. B* **2009**, *90*, 516.
[5] L. T. Qin, X. R. Pang, H. H. Zeng, Y. P. Liang, L. Y. Mo, D. Q. Wang, J. F. Dai, *Sci. Total Environ.* **2020**, *708*, 134552.
[6] S. Feizpoor, A. Habibi-Yangjeh, R. Luque, *Chemosphere* **2023**, *336*, 139101.
[7] X. L. Zou, T. Zhou, J. Mao, X. H. Wu, *Chem. Eng. J.* **2014**, *257*, 36.
[8] K. M. S. Hansena, A. Spiliotopouloub, R. K. Chhetria, M. E. Casasc, K. Besterc, H. R. Andersena, *Chem. Eng. J.* **2016**, *290*, 507.
[9] D. M. Ma, Y. Yang, B. F. Liu, G. J. Xie, C. Chen, N. Q. Ren, D. F. Xing, *Chem. Eng. J.* **2021**, *408*, 127992.
[10] C. Q. Tan, X. C. Jian, Y. J. Dong, X. Lu, X. Y. Liu, H. M. Xiang, X. X. Cui, J. Deng, H. Y. Gao, *Chem. Eng. J.* **2019**, *359*, 594.
[11] L. Wang, L. X. You, J. M. Zhang, T. Yang, W. Zhang, Z. X. Zhang, P. X. Liu, S. Wu, F. Zhao, J. Ma, *J. Hazard. Mater.* **2018**, *360*, 402.
[12] H. F. Fu, Z. Y. Feng, S. S. Liu, P. Wang, C. Zhao, C. C. Wang, *Chin. Chem. Lett.* **2023**, *34*, 107425.
[13] J. H. Wang, R. Abazari, S. Sanati, A. Ejsmont, J. Goscianska, Y. T. Zhou, D. P. Dubal, *Small* **2023**, *19*, 2300673.
[14] C. Jia, T. He, G. M. Wang, *Coord. Chem. Rev.* **2023**, *476*, 214930.
[15] Y. W. Gao, S. M. Li, Y. X. Li, L. Y. Yao, H. Zhang, *Appl. Catal. B* **2017**, *202*, 165.
[16] M. Peñas-Garzón, M. J. Sampaio, Y. L. L. Wang, J. Bedia, J. J. Rodriguez, C. Belver, C. G. Silva, J. L. Faria, *Sep. Purif. Technol.* **2022**, *286*, 120467.
[17] Y. Tang, X. L. Li, H. Zhang, T. W. Ouyang, Y. Jiang, M. M. Mu, X. H. Yin, *Chemosphere* **2020**, *259*, 127431.
[18] G. H. Zhong, D. X. Liu, J. Y. Zhang, *J. Mater. Chem. A* **2018**, *6*, 1887.
[19] G. M. Rain, S. M. Ghoreishian, K. S. Ranjith, S. H. Park, M. Lee, R. Umapathi, Y. K. Han, Y. S. Huh, *Adv. Mater. Technol.* **2023**, *8*, 2300685.
[20] Y. B. Li, Z. L. Jin, T. S. Zhao, *Chem. Eng. J.* **2020**, *382*, 120051.
[21] Y. Wu, X. M. Li, Q. Yang, D. B. Wang, F. B. Yao, J. Cao, Z. Chen, X. D. Huang, Y. Yang, X. P. Li, *Chem. Eng. J.* **2020**, *390*, 124519.
[22] R. W. Liang, S. G. Luo, F. F. Jing, L. J. Shen, N. Qin, L. Wu, *Appl. Catal. B* **2015**, *176*, 240.
[23] I. Khan, A. H. Yuan, S. Khan, A. Khan, S. Khan, S. A. Shah, M. S. Luo, W. Yaseen, X. P. Shen, M. Yaseen, *ACS Appl. Nano Mater.* **2022**, *5*, 13404.

[24] R. Levinson, P. Berdahl, H. Akbari, *Sol. Energy Mater. Sol. Cells* **2012**, *107*, 337.
[25] D. D. Li, S. H. Yu, H. L. Jiang, *Adv. Mater.* **2018**, *30*, 1707377.
[26] Y. X. Zhuang, D. R. Chen, W. J. Chen, W. X. Zhang, X. Su, R. R. Deng, Z. F. An, H. M. Chen, R. J. Xie, *Light Sci. Appl.* **2021**, *10*, 132.
[27] M. Yu, X. Lv, A. M. Idris, S. Li, J. Lin, H. Lin, J. Wang, Z. Li, *J. Colloid Interface Sci.* **2022**, *612*, 782.
[28] F. Wang, X. G. Liu, *Chem. Soc. Rev.* **2009**, *38*, 976.
[29] Y. P. Wu, Z. Z. Cheng, X. H. Ling, L. L. Peng, C. H. Deng, *Mater. Res. Bull.* **2023**, *163*, 112232.
[30] B. Jin, S. Wang, M. Lin, Y. Jin, S. Zhang, X. Cui, Y. Gong, A. Li, F. Xu, T. J. Lu, *Biosens. Bioelectron.* **2017**, *90*, 525.
[31] H. Zhu, Y. Yang, Y. Kang, P. Niu, X. Kang, Z. Yang, H. Ye, G. Liu, *J. Mater. Sci. Technol.* **2022**, *102*, 1.
[32] Z. J. Wang, C. Wang, Q. Y. Han, G. Wang, M. D. Zhang, J. Zhang, W. Gao, H. R. Zheng, *Mater. Res. Bull.* **2017**, *88*, 182.
[33] N. Liu, W. P. Qin, G. S. Qin, T. Jiang, D. Zhao, *ChemComm.* **2011**, *47*, 7671.
[34] Z. Li, O. Johnson, J. Huang, T. Feng, C. Yang, Z. Liu, W. Chen, *Mater. Res. Bull.* **2018**, *106*, 365.
[35] H. Hu, B. Guan, B. Xia, X. W. Lou, *J. Am. Chem. Soc.* **2015**, *137*, 5590.
[36] F. Wang, X. Liu, *J. Am. Chem. Soc.* **2008**, *130*, 5642.
[37] P. Dai, Y. Yao, E. Hu, D. Xu, Z. Li, C. Wang, *Appl. Surf. Sci.* **2021**, *546*, 149128.
[38] J. Tang, Y. Liu, J. Q. Hu, S. B. Zheng, X. C. Wang, H. P. Zhou, B. K. Jin, *Microchem. J.* **2020**, *155*, 104759.
[39] M. A. Lafta, S. H. Ammar, *Mater. Sci. Semicond. Process* **2023**, *153*, 107131.
[40] T. He, Y. Liu, S. Q. Zhang, C. H. Meng, L. Li, H. Wang, D. S. Zhen, *J. Nanopart Res.* **2023**, *25*, 160.
[41] S. Li, M. Zhang, Z. Qu, X. Cui, Z. Liu, C. Piao, S. Li, J. Wang, Y. Song, *Chem. Eng. J.* **2020**, *382*, 122394.
[42] M. Hosny, M. Fawzy, A. S. Eltaweil, *J. Environ. Manage.* **2022**, *316*, 115238.
[43] M. Kohantorabi, S. Giannakis, G. Moussavi, M. Bensimon, M. R. Gholami, C. Pulgarin, *J. Hazard. Mater.* **2021**, *413*, 125308.
[44] M. J. Tou, Y. Y. Mei, S. Bai, Z. G. Luo, Y. Zhang, Z. Q. Li, *Nanoscale* **2016**, *8*, 553.
[45] H. H. Ren, F. H. Huang, J. M. Jiang, L. Wang, J. L. Zhang, *Chem. Eng. J.* **2022**, *427*, 132023.
[46] K. Du, X. Xu, S. Yao, P. Lei, L. Dong, M. Zhang, J. Feng, H. Zhang, *CrystEngComm.* **2018**, *20*, 1945.
[47] Z. G. Gao, J. Q. Zhang, S. J. Zhang, J. Wang, Y. H. Song, *Chem. Eng. J.* **2021**, *421*, 127829.
[48] J. N. Qin, S. B. Wang, X. C. Wang, *Appl. Catal. B* **2017**, *209*, 476.
[49] X. X. Sun, W. W. Xu, X. Q. Zhang, T. Z. Lei, S. Y. Lee, Q. L. Wu, *J. Energy Chem.* **2021**, *52*, 170.
[50] C. Yuan, P. F. Cheng, J. Li, X. L. Gao, X. S. Gao, X. Wang, M. L. Jin, R. Nötzel, G. F. Zhou, Z. Zhang, J. M. Liu, *Microporous Mesoporous Mater.* **2019**, *285*, 13.
[51] E. S. Elmorsy, W. A. Amer, A. Mahrous, M. M. Ayad, *Mater. Sci. Eng. B* **2023**, *298*, 116900.
[52] X. Y. Guo, C. F. Chen, D. Q. Zhang, C. P. Tripp, S. Y. Yin, W. P. Qin, *RSC Adv.* **2016**, *6*, 8127.
[53] K. L. Zhang, M. Zhou, C. L. Yu, K. Yang, X. X. Li, S. Yang, J. Guan, W. X. Dai, W. Y. Huang, *J. Mater. Sci.* **2020**, *55*, 10435.
[54] F. Liu, S. C. Zhang, D. Xu, F. Sun, W. L. Wang, X. Y. Li, W. S. Yu, X. T. Dong, G. X. Liu, H. Yu, *J. Alloys Compd.* **2022**, *929*, 167330.
[55] S. Singh, V. Takhar, S. H. Nannuri, S. D. George, R. Banerjee, S. K. Misra, *ACS Appl. Nano Mater.* **2023**, *6*, 10441.
[56] P. H. Bell, R. O. Roblin Jr., *J. Am. Chem. Soc.* **1942**, *64*, 2905.
[57] A. P. S. Batista, F. C. C. Pires, A. C. S. C. Teixeira, *J. Photochem. Photobiol. A* **2014**, *290*, 77.
[58] Q. L. Zeng, J. Sun, X. Y. Bai, Z. B. Xu, *J. Clean. Prod.* **2023**, *396*, 136495.
[59] Z. Wang, J. Cao, F. Meng, *Water Res.* **2015**, *68*, 404.
[60] M. M. Zhao, X. Y. Bai, Y. P. Zhang, Y. Yuan, J. Sun, *J. Hazard. Mater.* **2022**, *430*, 128350.
[61] G. Fang, C. Zhu, D. D. Dionysiou, J. Gao, D. Zhou, *Bioresour. Technol.* **2015**, *176*, 210.
[62] H. Li, T. F. Li, S. T. He, J. Zhou, T. C. Wang, L. Y. Zhu, *Chem. Eng. J.* **2020**, *395*, 125091.
[63] J. Hang, X. H. Yi, C. C. Wang, H. F. Fu, P. Wang, Y. Zhao, *J. Hazard. Mater.* **2022**, *424*, 127415.
[64] H. Y. Zhan, Q. X. Zhou, M. M. Li, R. R. Zhou, Y. S. Mao, P. F. Wang, *Appl. Catal. B* **2022**, *310*, 121329.
[65] Q. Su, J. Li, H. Y. Yuan, B. Wang, Y. H. Wang, Y. C. Li, Y. Xing, *Chem. Eng. J.* **2022**, *427*, 131594.
[66] Y. Duan, L. Deng, Z. Shi, X. Liu, H. Zeng, H. Zhang, J. Crittenden, *J. Colloid Interface Sci.* **2020**, *561*, 696.
[67] J. F. Yang, M. He, T. F. Wu, A. P. Hao, S. B. Zhang, Y. D. Chen, S. B. Zhou, L. Y. Zhen, R. Wang, Z. L. Yuan, L. Deng, *Chem. Eng. J.* **2018**, *349*, 56.
[68] X. Y. Guo, C. F. Chen, D. Q. Zhang, C. P. Tripp, S. Y. Yin, W. P. Qin, *RSC Adv.* **2016**, *6*, 8127.
[69] S. M. Lashgari, H. Yari, M. Mahdavian, B. Ramezanzadeh, G. Bahlakeh, M. Ramezanzadeh, *J. Taiwan Inst. Chem. Eng.* **2020**, *117*, 209.
[70] A. M. Tanvi, R. K. Bedi, S. Kumar, V. Saxena, A. Singh, D. K. Aswal, *RSC Adv.* **2016**, *6*, 48064.
[71] Y. J. Meng, L. X. Zhang, H. F. Jiu, Q. L. Zhang, H. Zhang, W. Ren, Y. Sun, D. T. Li, *Mater. Sci. Semicond. Process.* **2019**, *95*, 35.
[72] Y. B. Li, Z. L. Jin, T. S. Zhao, *Chem. Eng. J.* **2020**, *282*, 120051.
[73] X. J. Wen, Q. Lu, X. X. Lv, J. Sun, J. Guo, Z. H. Fei, C. G. Niu, *J. Hazard. Mater.* **2020**, *385*, 121508.
[74] D. P. Sun, D. C. Yang, P. Wei, B. Liu, Z. G. Chen, L. Y. Zhang, J. Lu, *ACS Appl. Mater. Interfaces* **2020**, *12*, 41960.
[75] J. Li, G. Z. Xie, J. Jiang, Y. Y. Liu, C. X. Chen, W. X. Li, J. L. Huang, X. L. Luo, M. Xu, Q. P. Zhang, M. Yang, Y. J. Su, *Nano Energy* **2023**, *108*, 108234.
[76] J. B. Zhao, Z. D. Lu, Y. D. Yin, C. McRae, J. A. Piper, J. M. Dawes, D. Y. Jin, E. M. Goldys, *Nanoscale* **2013**, *5*, 944.
[77] H. J. Cai, T. T. Shen, J. Zhang, C. F. Shan, J. G. Jia, X. Li, W. S. Liu, Y. Tang, *J. Mater. Chem. B* **2017**, *5*, 2390.
[78] R. Balaji, S. Kumar, K. L. Reddy, V. Sharma, B. K., V. Krishnan, *J. Alloys Compd.* **2017**, *724*, 481.
[79] M. He, X. C. Pang, X. Q. Liu, B. B. Jiang, Y. J. He, H. Snaith, Z. Q. Lin, *Angew. Chem. Int. Ed.* **2016**, *55*, 4280.
[80] Y. T. Li, J. L. Tang, L. C. He, Y. Liu, Y. L. Liu, C. Y. Chen, Z. Y. Tang, *Adv. Mater.* **2015**, *27*, 4075.